Gap Flows through Idealized Topography. Part II: Effects of Rotation and Surface Friction

SAŠA GABERŠEK* AND DALE R. DURRAN

Department of Atmospheric Sciences, University of Washington, Seattle, Washington

(Manuscript received 9 September 2005, in final form 1 February 2006)

ABSTRACT

Numerical simulations are conducted of geostrophically balanced flow over an isolated mountain cut by a horizontal gap. The relative importance of the along-gap synoptic-scale pressure gradient and terrain-induced mesoscale circulations for the generation of gap winds was examined by changing the direction of the synoptic-scale wind relative to the topography. In all cases, the forcing associated with mesoscale circulations generated by the mountain was at least as significant as the synoptic-scale pressure gradient. In the cases where a component of the large-scale flow was directed perpendicular to the ridge, the dynamics were dominated by either the vertical momentum fluxes due to mountain lee waves or by mesoscale pressure gradients associated with upstream blocking or lee troughing. Mesoscale circulations were also important when the large-scale flow was parallel to the ridge because surface friction turned the low-level winds toward the high pressure side of the ridge, partially blocking the flow and enhancing the along-gap pressure gradient.

The flow in the interior of a very long uniform gap was also simulated for a case with the synoptic-scale winds parallel to the ridge so that the synoptic-scale pressure gradient was down the gap. The flow in the interior of the long gap was not horizontal and not in a simple dynamical balance between acceleration, the pressure gradient force, and surface friction. Even the flow in the lowest 150 m was gradually subsiding. Subsidence and lateral momentum flux convergence at low levels near the center of the gap were important contributors to the mass and along-gap momentum budgets.

1. Introduction

Strong winds blowing through gaps in mountain ranges or between islands have been observed in many parts of the world. These "gap winds" occur in the presence of along-gap pressure gradients, which can be produced directly by variations in the synoptic-scale pressure field, by locally induced mesoscale pressure perturbations, or by a combination of both. One major goal of this paper is to assess the relative importance of synoptic and terrain-induced mesoscale pressure gradients in forcing strong gap flow.

The large-scale geostrophically balanced pressure gradient has been identified as the primary agent forcing gap flow in the Shelikof Strait in Alaska (Lackmann and Overland 1989) and Lake Torneträsk in Sweden (Smedman and Bergström 1995). The underlying dynamics, in which topographically constrained ageostrophic winds blow along the gap from high to low pressure, was named "pressure driven channeling" by Whiteman and Doran (1993), who found it to be the dominant mechanism for generating light or moderate winds within the relatively broad Tennessee Valley. Idealized gap winds driven by the large-scale pressure gradient have also been simulated by Sprenger and Schär (2001), who examined a stratified geostrophically balanced westerly flow parallel to the axis of an infinitely long east–west ridge transected by a north–south gap with a col. They found that southerly gap winds could occur in free-slip simulations provided the col was low enough to create a deep cross-mountain pathway.

Zängl (2002a) extended the work of Sprenger and Schär (2001) to the case of geostrophically balanced westerly flow parallel to an east–west ridge of *finite* length cut by a north–south gap. He found that meso-

* Current affiliation: Faculty of Mathematics and Physics, University of Ljubljana, Ljubljana, Slovenia.

Corresponding author address: Dr. Dale R. Durran, Department of Atmospheric Sciences, University of Washington, Box 351640, Seattle, WA 98195.
E-mail: durrand@atmos.washington.edu

© 2006 American Meteorological Society

scale circulations created by the interaction of the large-scale flow and the isolated ridge exerted a dramatic influence on the gap winds. In free-slip simulations, the tendency for strong anticyclonic flow around the mountain reversed the total along-gap pressure gradient to create northerly gap flow. Zängl (2002a) also found that, when surface friction was included in the simulations, the low-level winds turned toward low pressure and, in doing so, they also turned toward the southern side of the mountain. When these low-level winds were blocked by the southern flanks of the topography, the synoptic-scale along-gap pressure gradient was reinforced and southerly gap flow developed directly opposite to the direction of the flow in the corresponding free-slip case.

Zängl (2002b) and Gaberšek and Durran (2004, hereafter GD04) have also conducted idealized simulations of stratified flow perpendicular to finite ridges cut by a transverse gap, with the gap parallel to the oncoming flow. Except for a couple of the simulations in Zängl (2002b), these studies neglected the Coriolis force and surface friction. These papers, along with an earlier study of flow perpendicular to an infinite ridge periodically cut by a series of transverse cols by Saito (1993), demonstrate that cross-mountain winds can produce large mesoscale perturbations, such as mountain waves, lee troughs, and upstream blocking, that are capable of driving strong gap winds. In this paper we generalize the situations considered in Zängl (2002a,b) and GD04 to consider the relative contribution of synoptic-scale pressure gradients and mesoscale perturbations in geostrophically balanced flows striking a long, but finite, ridge at several different angles. The ridge is cut by a narrow transverse gap with a flat bottom (no col). Surface friction is included in most of our simulations.

The observational studies motivating this work include, on one hand, the previously noted examples where gap flow appears to be primarily driven by the large-scale pressure gradient (pressure driven channeling). On the other hand, mesoscale circulations in the form of mountain waves were found to play a major role in enhancing gap winds along the Taku River in Alaska (Colman and Dierking 1992) and in the Strait of Juan de Fuca (Colle and Mass 2000). In particular, Colle and Mass observed significant mesoscale modulation of the gap flow in Doppler radar data collected in the Strait of Juan de Fuca and linked those observations to real-data simulations with the fifth-generation Pennsylvania State University–National Center for Atmospheric Research Mesoscale Model (MM5) showing subsidence and acceleration near the gap exit. There are also many observations of flow through passes in mountains in which mesoscale circulations appear to play a dominant role, including easterly winds through the Stampede Pass in Washington State (Colle and Mass 1998a,b), northerly winds through Chivela Pass, Mexico (Steenburgh et al. 1998), and southerly föhn winds in the Wipp Valley of Austria (Flamant et al. 2002; Gohm and Mayr 2004).

Our focus on geostrophically balanced pressure gradients allows a concise treatment of one fundamental idealized weather pattern, but it should be noted that in many real-world events, the mountains support significant cross-ridge temperature contrasts. In such cases the synoptic conditions responsible for the along-gap pressure gradient are not primarily related to geostrophic balance with respect to the upper-level flow, but rather are generated hydrostatically by the low-level temperature contrasts across the mountain. Examples where strong temperature contrasts play a significant role in creating or reinforcing gap flow include all of the examples mentioned in the previous paragraph as well as easterly winds in the Columbia River Gorge (Sharp and Mass 2004), and Howe Sound, British Columbia (Jackson and Steyn 1994a,b). The additional influence of such cross-mountain temperature gradients on the along-gap synoptic pressure gradient is not included in these simulations and is left for future work.

Many previous simple theories of flow through level gaps have supposed that the flow is essentially horizontal. As noted in GD04, however, Bernoulli's theorem for the compressible atmosphere implies that, if there is an increase in wind speed along a *horizontal* trajectory in steady inviscid flow, then the temperature must decrease along that trajectory. Since the temperature and the wind speed both increase between the entrance and exit in many quasi-steady real-world gap-wind events, the bulk of the accelerating current must either subside or be subject to sufficient dissipation to render Bernoulli's equation irrelevant. Substantial subsidence was indeed present in the strong gap-wind cases examined in GD04, but surface friction was neglected in those simulations. A second major goal of this paper is, therefore, to determine the extent to which subsidence continues to play a significant role in the generation of strong horizontal gap flows when surface friction is present.

The paper is structured as follows: the setup for the numerical experiments is described in section 2. The strength and structure of the simulated gap flows are presented in section 3, along with an examination of the relative importance of geostrophic and mesoscale forcing. Section 4 explores the kinematics of these gap flows through an analysis of the mass budget along the gap. Flow dynamics are explored in section 5 on the basis of

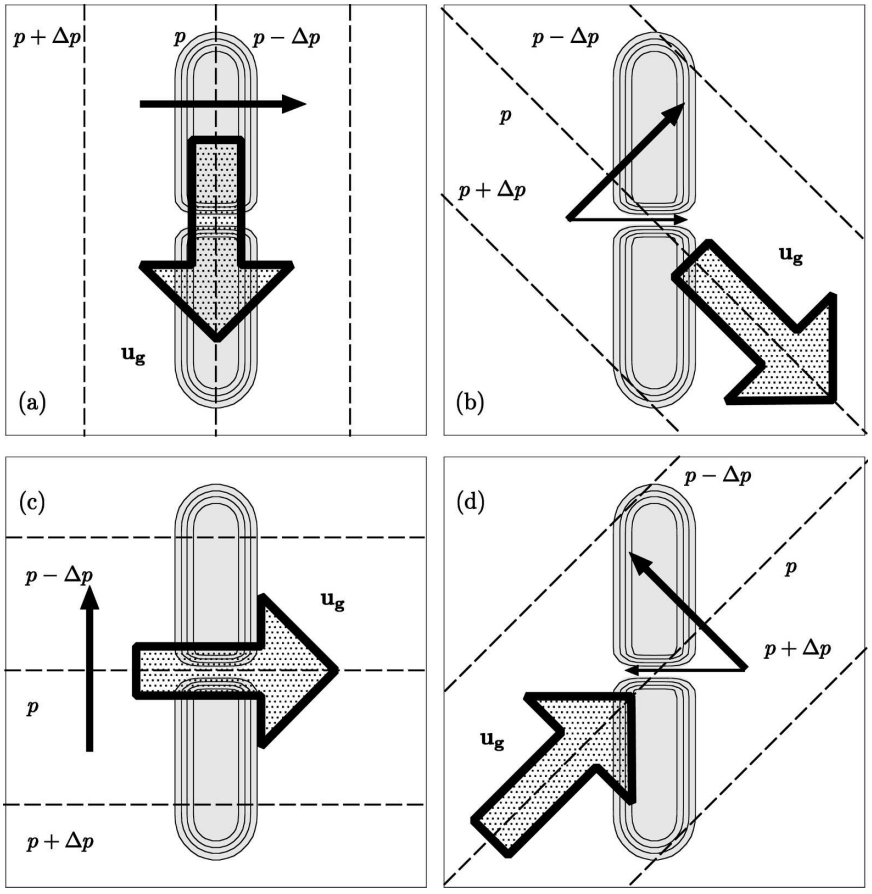

FIG. 1. Geostrophic wind (large open arrow) and pressure gradient (thick solid arrow) relative to the 1.4-km-high topography (shaded, with contours every 300 m). Dashed lines are isobars of the synoptic-scale pressure field and thin arrows show the component of the geostrophic pressure gradient parallel to the gap axis. Flow is from the (a) north, (b) northwest, (c) west, and (d) southwest.

the along-gap momentum budget. Section 6 explores the kinematics and dynamics of gap flow in the central region of a very long uniform gap. Conclusions are presented in section 7.

2. Experimental setup

The numerical model used in these simulations is the same one used in GD04 except that the Coriolis force is included and most simulations also incorporate surface friction. The surface friction parameterization is based on a simplified version of Blackadar's first-order closure (Zhang and Anthes 1982). Details concerning the implementation of these additions to the model are given in the appendixes.

The basic meteorological scenario consists of a uniform geostrophically balanced flow impinging upon an isolated ridge at some arbitrary angle. The topography is a ridge parallel to the y axis with semicircular ends and a gap in the center running perpendicular to the ridgeline, as illustrated by Fig. 1. The ridge is defined such that

$$r(x, y) = \begin{cases} \dfrac{h_0}{16}\left[1 + \cos\left(\dfrac{\pi s}{4a}\right)\right]^4, & s \le 4a \\ 0, & \text{otherwise,} \end{cases} \tag{1}$$

where

$$s = \begin{cases} \max(0, |x| - b), & |y| \le c \\ \max(0, [x^2 + (|y| - c)^2]^{1/2} - b), & \text{otherwise.} \end{cases}$$

A gap, defined by

$$g(y) = \begin{cases} 0, & |y| \le d/2 \\ \sin\left(\dfrac{\pi(|y| - d/2)}{2e}\right), & d/2 < |y| \le e + d/2 \\ 1, & \text{otherwise,} \end{cases} \tag{2}$$

is cut into the ridge such that the total topography is given by the product $h(x, y) = r(x, y)g(y)$. Both gap and ridge are centered at $(x, y) = (0, 0)$. In all cases, the y dimension of the ridge is $c = 90$ km and the width of the bottom of the gap is $d = 10$ km. The other terrain-related parameters, which differ among the various simulations, are the height of the ridge h_0, the half-widths of the sloped a and flat-topped b sections of the ridge, and the horizontal distance over which the sidewalls rise from the bottom of the gap to the ridgeline e.

The simulations are initialized with uniform winds of speed U coming from one of four directions: north, northwest, west, or southwest. In all cases, the Brunt–Väisälä frequency is an initially uniform value of $N = 0.01\ \mathrm{s}^{-1}$. The two basic gap-flow regimes identified in GD04 are considered for each flow direction. The *mountain wave* regime, for which $\epsilon \equiv Nh_0/U = 1.4$, is examined using simulations in which $U = 10\ \mathrm{m\ s}^{-1}$ and $(h_0, a, b, e) = (1.4, 10, 10, 5)$ km. The topography in this case is the same as that considered in GD04. The *upstream-blocking* regime, with $\epsilon = 5.0$, is obtained when $U = 5\ \mathrm{m\ s}^{-1}$ and $(h_0, a, b, e) = (2.5, 15, 0, 10)$ km. The topography below $z = 1.2$ km is very similar in all of these simulations and includes a gap roughly 40 km long and 10 km wide. One additional "long-gap" simulation is conducted with $10\ \mathrm{m\ s}^{-1}$ flow from the north and $(h_0, a, b, e) = (1.4, 10, 70, 5)$ km. In all cases, the horizontal wind field is "turned on" instantaneously and integrated to a nondimensional time $T \equiv Ut/a = 40$, by which point the flow in the vicinity of the topography reaches a nearly steady state.

The simulations use a set of four nested grids. Each of the three largest grids covers a square domain with the gap at its center. The spatial and temporal resolution is refined by a factor of 3 in each nest. The finest grid, on which $\Delta x = 0.5$ km, covers the gap itself. Except for the long-gap case, the $x \times y$ dimension of this grid is 81.5 km $\times$ 27.5 km. The next coarsest mesh, on which $\Delta x = 1.5$ km, occupies a square 271 km on a side and is just large enough to include the entire mountain. The next grid, having $\Delta x = 4.5$ km, covers a square 405 km on a side. The outer grid, for which $\Delta x = 13.5$ km, extends over a 1269 km $\times$ 1269 km square. The domain is 13 km deep with the lowest grid level for all variables (except w) located at $z = 50$ m. The vertical grid spacing varies, starting at 100 m in the layer $0 \leq z < 3$ km, then smoothly increasing to 250 m over the layer $3 \leq z < 4$ km, and remaining constant at 250 m above 4 km. This vertically stretched grid allows us to efficiently resolve both the low-level gap flow and any mountain waves that might develop aloft. Surface values of u, v, and θ are also computed via the boundary layer parameterization at $z = 10$ m.

3. Geostrophic or mesoscale forcing?

The geostrophic pressure gradients associated with large-scale flows from the north, northwest, west, and southwest are shown by the solid heavy arrows in Fig. 1, with the component of each gradient along the gap indicated by thin solid arrow. The along-gap geostrophic pressure gradient is strongest in the north-flow (hereafter N-flow) case, so if gap flow is driven exclusively by the geostrophic pressure field (pressure driven channeling), the gap winds should be strongest in the N-flow case. In contrast to the other three cases, the along-gap geostrophic pressure gradient in the southwest-flow (SW-flow) case is east to west. If pressure driven channeling dominates the gap flow in that case, the winds should be easterly. Does the large-scale geostrophic pressure gradient actually drive the flow within the gap in these idealized cases?

Zängl (2002a,b) and GD04 found that terrain-induced mesoscale disturbances, such as mountain waves or upstream blocking, could force significant gap flows. The NW, W, and SW cases are more favorable than the N-flow case for producing strong mountain waves or upstream blocking in the vicinity of the gap, and the resulting mesoscale perturbations would favor the generation of westerly gap flow in all three of these cases. Thus, rather different gap flows should be generated in response to the large-scale pressure gradient and the mesoscale forcing in the four prototypical cases shown in Fig. 1, and these cases provide a concise way to compare the relative importance of these two mechanisms.

a. Mountain wave regime

First, consider the gap winds that develop in the mountain wave regime with $\epsilon = 1.4$. Figure 2 shows the pressure field and streamlines at $z = 300$ m for simulations of each of the four cases schematically illustrated in Fig. 1. The pressure is plotted as the perturbation with respect to the undisturbed hydrostatic pressure at the center of the gap. The zero pressure perturbation contour is indicated by a heavy dot–dashed curve. In the absence of the topography, a uniform gradient in this perturbation pressure would balance the geostrophic wind and the zero pressure contour would be a straight line passing through the center of the gap. Away from the mountain the isobars are parallel to the upper-level winds and, as apparent in Fig. 2, the 300-m-level streamlines angle across the isobars toward lower pressure due to surface friction. Both the pressure field and the streamlines are highly perturbed near the mountain. In all except the N-flow case, mountain-induced mesoscale disturbances increase the

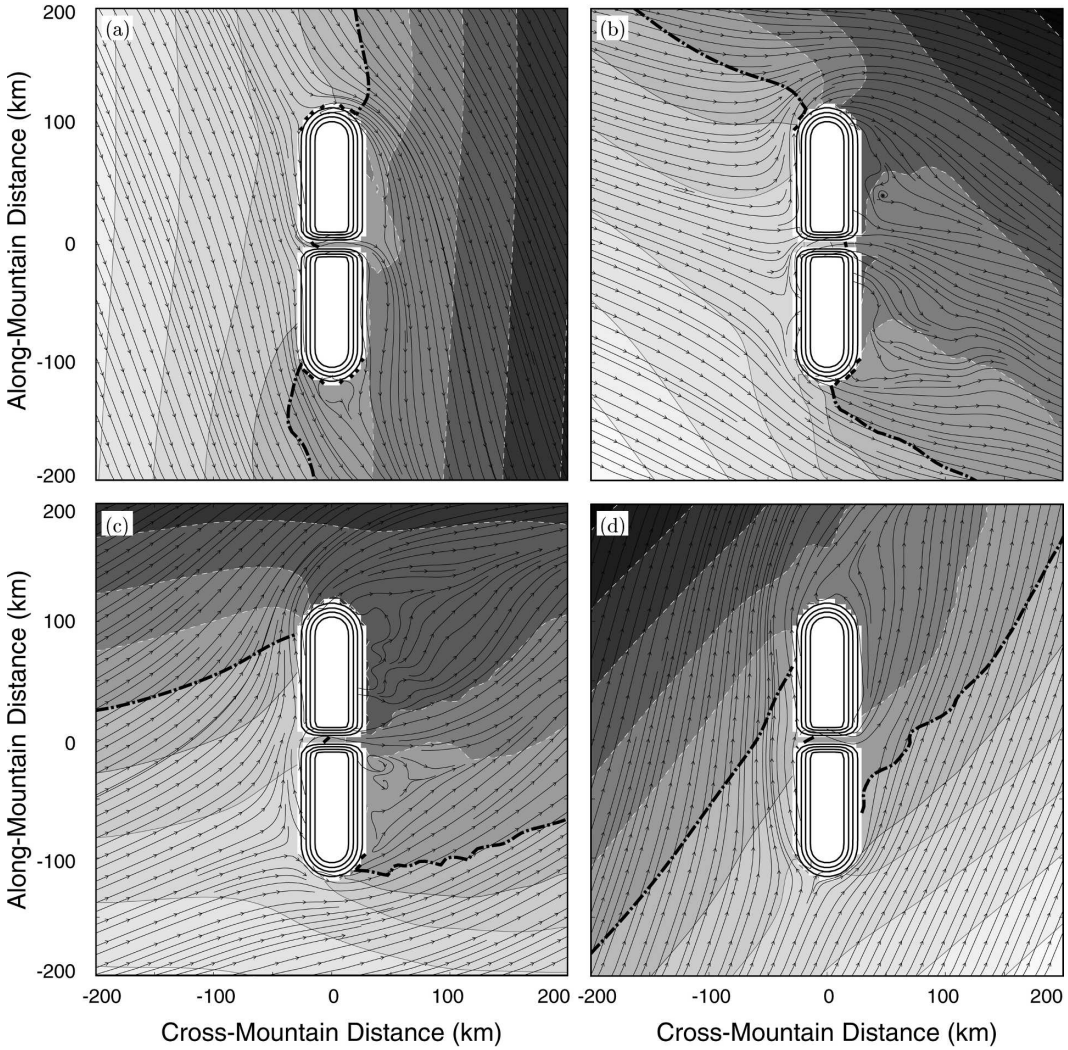

FIG. 2. Horizontal cross sections at $z = 0.3$ km for flows from the (a) N, (b) NW, (c) W, and (d) SW with $\epsilon = 1.4$ at $T = 40$. Pressure perturbation, including a synoptic part supporting the geostrophic flow, is plotted at a contour interval (CI = 60 Pa) and shading ranging from dark (negative values) to light (positive values); the pressure perturbation is zero along the thick black dot–dashed contour. Horizontal streamlines are superimposed. Terrain contours are every 300 m.

pressure on the upstream side of the gap and decrease it downstream.

In the N-flow case (Fig. 2a), surface friction turns the low-level flow toward the western slopes of the ridge. As this turned flow is blocked by the topography, the pressure along the western flank of the mountain rises and the west-to-east pressure gradient along the gap is enhanced. The resulting westerly gap flow at $z = 300$ m (Fig. 3b) exceeds the speed of the background geostrophic northerlies (10 m s^{-1}). The importance of surface friction and the role of boundary layer turning in generating gap winds when the large-scale flow is parallel to the long axis of the topography has been previously noted by Zängl (2002a). In addition to enhancing the low-level west-to-east pressure gradient in the gap, surface friction also helps decouple the low-level gap flow from the upper-level northerlies blowing along the ridgeline. In the absence of such decoupling, the northerly winds in the free-slip simulation sweep down into the gap and form a complex pattern of horizontal eddies within the gap itself, as shown in Fig. 3a, which shows the same data plotted in Fig. 3b except for a free-slip N-flow simulation.

The nature of the decoupling of the gap flow from the overlying northerlies induced by surface friction is further illustrated in Fig. 4, which shows isentropes and contours of u in a y–z vertical cross section across the gap along the centerline of the ridge (at $x = 0$) for the

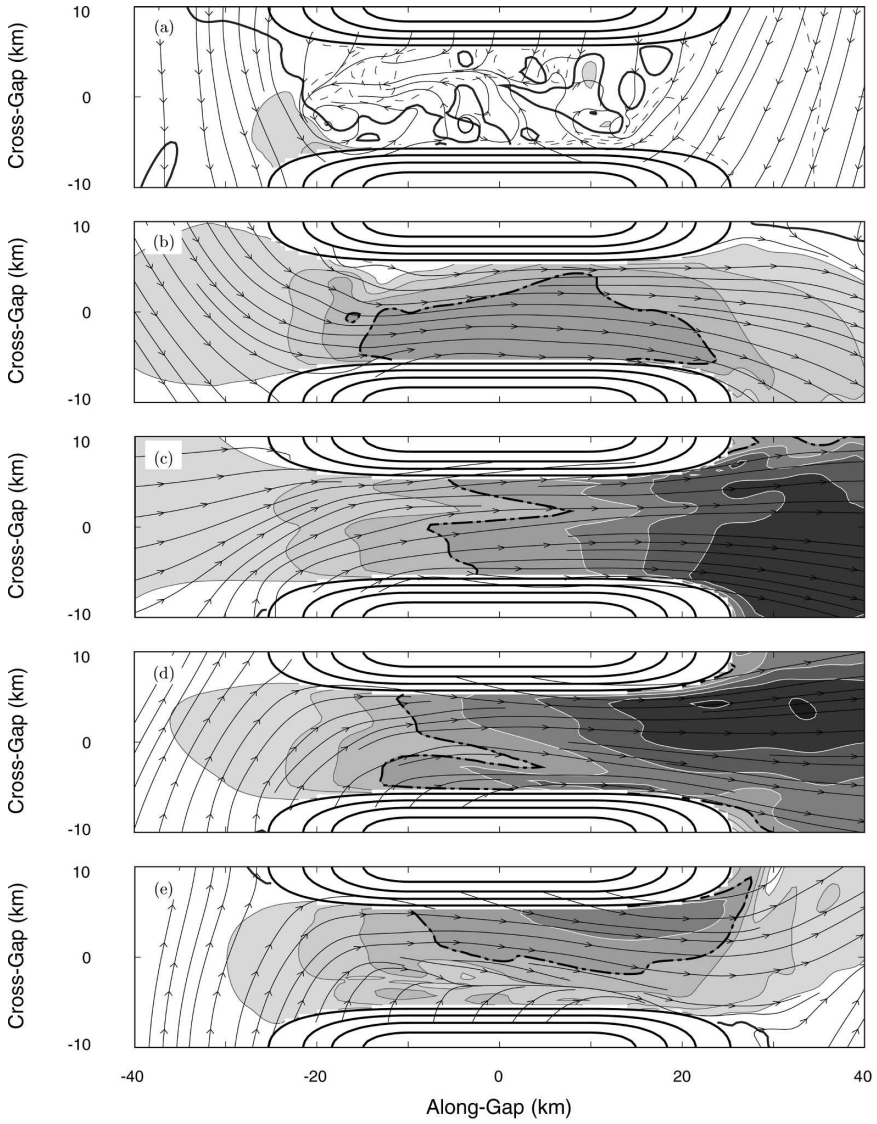

FIG. 3. Horizontal cross sections through the gap showing streamlines and u-component velocities at $z = 0.3$ km for (a) free-slip flow from the N and for (b) N, (c) NW, (d) W, and (e) SW flow with surface friction. In all cases $\epsilon = 1.4$, $T = 40$, and the terrain contours are shown by heavy black lines (CI = 300 m). Shades of gray indicate the u component of velocity (CI = 2.5 m s^{-1}) from light (low positive speeds) to dark shades (high speeds). Velocities less than 2.5 m s^{-1} are not shaded; negative velocities are indicated by dashed contour lines. The 10 m s^{-1} and zero contours are shown by heavy dot–dashed and solid lines, respectively. This plotting convention is used to display all contours of u or v shown in subsequent figures.

standard no-slip simulation and an otherwise identical free-slip case. In the free-slip case (Fig. 4a), a strong mountain wave develops in the northerly flow above the northern side of the gap with downslope winds penetrating deep into the gap. Only weak winds ($-2.5 \leq u \leq 2.5$ m s^{-1}) are found within the gap itself. On the other hand, when surface friction is accounted for, the mountain waves are much weaker, and the along-ridge flow is decoupled from a 12.5 m s^{-1} jet of westerly winds within the gap (Fig. 4b).

Due to frictional turning, the 300-m winds in the NW case (Fig. 2b) approach the mountain more nearly perpendicular to the ridge and parallel to the gap axis than in the W case (Fig. 2c). The combined effects of surface friction and Coriolis forces lead to a very asymmetric distribution of the blocked low-level flow in the W case,

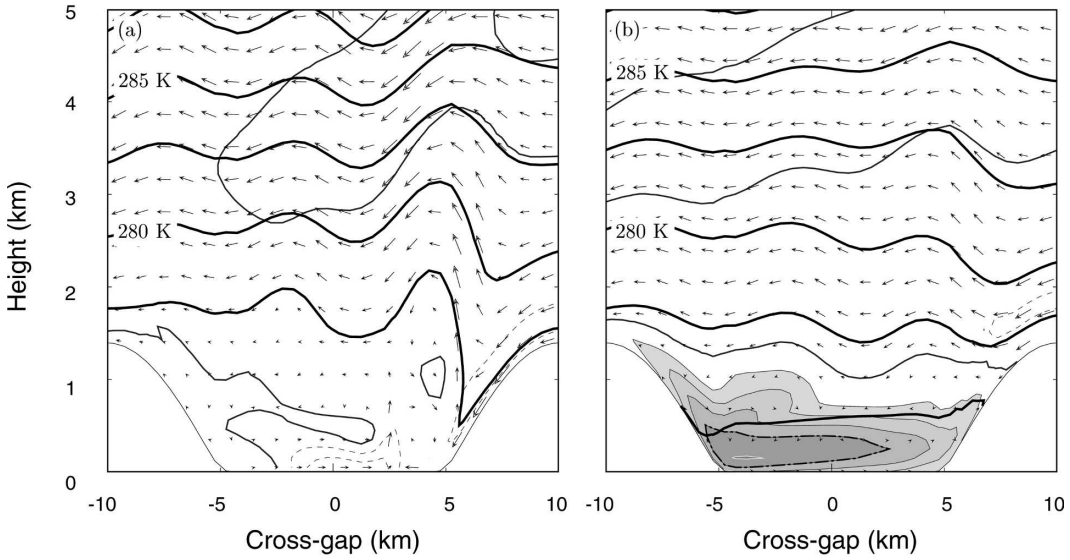

FIG. 4. Vertical cross sections at $x = 0$ km for northerly flows (from right to left): (a) free-slip and (b) with surface friction. In both cases $\epsilon = 1.4$ and $T = 40$. Gray shading is the same as in Fig. 3; the zero contour is the only contour present in (a). Heavy black lines are isentropes, CI = 2.5 K. Also shown are the v–w wind vectors in the plane of the cross section. The terrain profile is shown with a thin black line.

with flow splitting occurring near the southern edge of the mountain (Ólafsson and Bougeault 1997). In contrast, the splitting point lies near the center of the gap in the NW case. The location of the upstream splitting point in the NW and W cases varies as a function of the angle of the oncoming flow in a manner very similar to that obtained by Zängl (2004) for $\epsilon = 3$ flow over a mountain of roughly similar shape.

Much stronger gap winds develop in both the W and the NW cases; extensive regions with $u \geq 17.5$ m s^{-1} are present in the gap exit region and farther downstream (Figs. 3c,d). It is interesting to note that the distribution and magnitude of the high winds in the NW and W simulations are qualitatively similar to those observed by Doppler radar over the Strait of Juan de Fuca by Colle and Mass (2000) on 9 December 1995, although the synoptic situation on that day was far more complex than what we consider here. The 300-m winds in the W case are slightly stronger than those in the NW case despite the fact that the along-gap geostrophically balanced pressure gradient helps force gap winds in the NW case but is zero for westerly geostrophic flow. The strength of the gap flow in the W (and also the NW) case is due to the presence of a strong mountain wave in the cross-ridge flow, which transports westerly momentum into the gap from above. Strong mountain waves are apparent in the along-gap cross sections for both the NW-flow and W-flow cases shown in Figs. 5b,c. Note in particular how the descent of the 275-K and 277.5-K isentropes is associated with the acceleration of the low-level winds in both cases. Observations and an MM5 simulation of the 9 December 1995 event in the Strait of Juan de Fuca also show strong subsidence and evidence of mountain waves near the gap exit (Colle and Mass 2000).

Westerly gap winds also develop in the SW-flow case. Although the initial geostrophically balanced pressure gradient would force easterly flow, a weak westerly pressure gradient is produced along the gap by the mesoscale terrain-induced perturbations (Fig. 2d). Gap winds in excess of 12.5 m s^{-1} are found along the northern side of the gap (Fig. 3e). A modest mountain wave is apparent around the 4-km level in the vertical cross section in Fig. 5d, but the most important factor governing the winds in the gap is a much stronger mountain wave associated with southwest flow over the southern side of the gap. This wave is clearly evident in the y–z cross section at $x = -10$ km shown in Fig. 6. The lateral transport of high westerly momentum air into the gap by the southerly downslope winds plays an important role in accelerating the across-gap-averaged winds in the central section of the gap (as verified by the momentum budget presented in Fig. 13).

b. Upstream-blocking regime

The upstream-blocking regime is now investigated for the same four flow directions by increasing the mountain height from 1.4 to 2.5 km and decreasing the geostrophic wind from 10 to 5 m s^{-1} so that $\epsilon = 5.0$. Except in the N-flow case, mesoscale perturbations

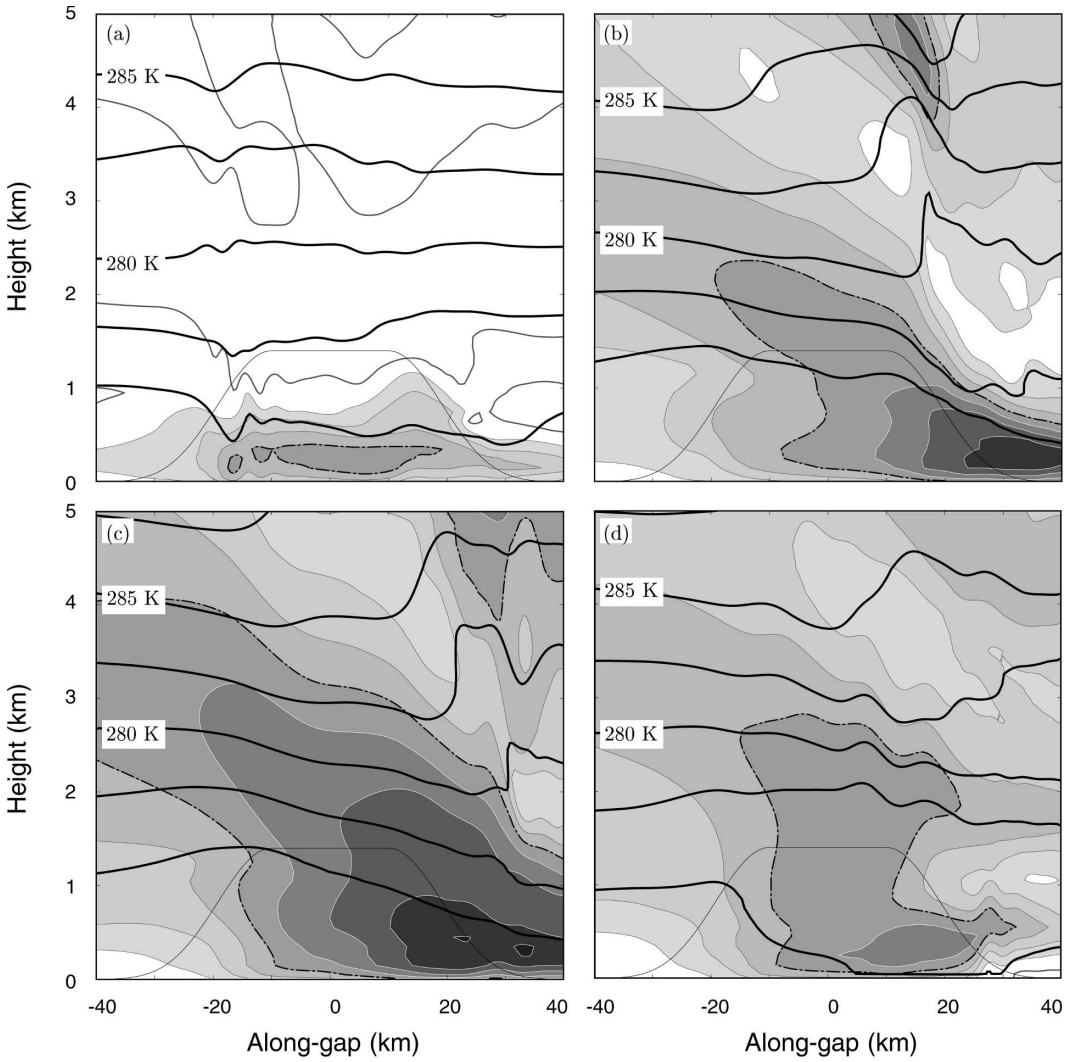

FIG. 5. Same as in Fig. 4 but at $y = 0$ km for flows from the (a) N and (b) NW, and at $y = 4$ km for (c) W and (d) SW. The ridge profile away from the gap is shown by the thin black line.

again increase the pressure upstream of the gap and lower it downstream relative to that which is in geostrophic balance with the undisturbed flow, as shown in Fig. 7. In comparison to the $\epsilon = 1.4$ simulations, the location of the zero-perturbation-pressure contour within the gap (shown by a short segment of the heavy dot–dashed line) moves upstream in all but the N-flow case. The upstream shift is particularly apparent for NW flow (cf. Figs. 2b and 7b). As will be discussed in section 5, this westward shift in the region of low pressure within the gap is associated with an increase in the pressure gradient in the gap entrance region.

In the N-flow case, surface friction turns the low-level wind toward the western slopes, producing modest blocking and enhancement of the pressure perturbations upstream. This is the same mechanism that was active in the $\epsilon = 1.4$ case. However, the second factor that was important when $\epsilon = 1.4$, frictionally induced decoupling of the gap flow from the northerly winds along the ridge top, is not active when $\epsilon = 5.0$; instead, there is sufficient flow splitting at the north end of the ridge to decouple the gap flow without any assistance from surface friction. As discussed by Zängl (2002a), the Coriolis force induces an anticyclonic bias in free-slip split flow so that the winds along the eastern flank of the ridge are supergeostrophic and are therefore deflected westward by the Coriolis force. Adiabatic cooling in the resulting upslope flow increases the pressure along the eastern side of the ridge and creates a very weak easterly gap flow (Fig. 8a). This easterly flow is opposite to that which occurs in the presence of surface friction (Fig. 8b) and is also opposite to that which

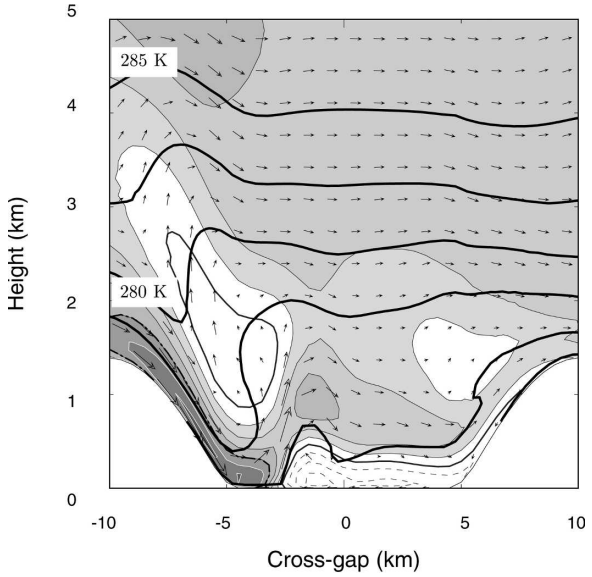

FIG. 6. Same as in Fig. 5 but at $x = -10$ km for the SW flow. The terrain profile is shown with a thin black line.

would be predicted based solely on the synoptic-scale pressure gradient.

The acceleration of the gap winds relative to the background pressure field in the N-flow simulation with surface friction is similar to that which develops when $\epsilon = 1.4$; however, since the geostrophic wind is only half as strong in the $\epsilon = 5$ simulation, the magnitude of the gap winds is weaker. The only contours that appear in the 300-m wind field plotted in Fig. 8b are 2.5 and 5 m s^{-1}.

Stronger winds are found in the three cases with a westerly component to the geostrophic flow, all of which produce some type of leeside vortex structure. The strongest winds, exceeding 12.5 m s^{-1}, occur in the NW and W cases (Figs. 8c,d). However, consistent with the structure of gap winds in the upstream-blocking regime noted in GD04, the high winds do not extend downstream from the gap as in the $\epsilon = 1.4$ simulations. The high wind region is even more tightly confined to the center of the gap in the SW case (Fig. 8e) in which the reversed circulation associated with the lee eddy, shown in Fig. 7d, penetrates well into the gap along the northern sidewall.

The maximum surface wind speeds (at $z = 10$ m) that develop within the gap and on the eastern slopes of the adjacent ridges in both the $\epsilon = 1.4$ and $\epsilon = 5$ simulations are compared in Table 1. Note that, in contrast to the speeds of the along-gap wind component plotted in most of the preceding figures, Table 1 gives the total wind speed, and in the $\epsilon = 1.4$ SW case the total wind includes a strong southerly component. Not surprisingly, very strong winds are present along the lee slopes in the mountain wave regime but not in the upstream blocking cases. Also listed in Table 1 is the relative enhancement of the gap or downslope wind speed $|\mathbf{v}|$ relative to the geostrophic wind U, defined as $(|\mathbf{v}| - U)/U$. The strongest relative enhancements occur in the gap in the NW, W, and SE $\epsilon = 5.0$ simulations. Since in actual atmospheric flows, flow blocking occurs under low-wind conditions, it seems unlikely that the strong relative enhancements evident in the $\epsilon = 5.0$ simulations would generate genuinely strong gap winds in real-world events.

4. Gap flow kinematics

We now consider the kinematics of these gap flows by analyzing mass fluxes through the three control volumes within the gap shown in Fig. 9. The top of each volume[1] is at 1.2 km and within the gap their width is the actual width of the gap. The upstream face of the upstream volume and downstream face of the downstream volume are $d + 2e$ wide, which according to (2) corresponds to the distance over which the uniform ridge is altered by the presence of the gap. The entrance, central, and exit volumes occupy the regions $-40 \le x \le -10$, $-10 \le x \le 10$, and $10 \le x \le 40$ km, respectively.

Let superscripts denote the coordinates that are fixed to define control-volume faces, and let subscripts "en," "c," or "ex" indicate fluxes into or out of the entrance, central, or exit volumes. The net lateral fluxes (through x–z planes) and the vertical fluxes are defined such that positive fluxes denote transport out of the volume. Arrows in the subscript denote the flux entering or exiting the control volume. Using this notation, the mass flux through the y–z plane between the entrance and central volume may be written as $\phi^x_{\rightarrow c}$. At steady state, the mass balances for each control volume can be expressed as

$$\phi^x_{\rightarrow c} = \phi^x_{\rightarrow en} - \phi^z_{en} - \phi^y_{en} \quad (3)$$

$$\phi^x_{c\rightarrow} = \phi^x_{\rightarrow c} - \phi^z_{c} \quad (4)$$

$$\phi^x_{ex\rightarrow} = \phi^x_{c\rightarrow} - \phi^z_{ex} - \phi^y_{ex} \quad (5)$$

Note that the sides of the gap prevent any lateral fluxes into the central volume and they reduce the y–z cross-sectional area of the central volume by a factor of

[1] The top was located at 1.2 km because the gap geometry below this level is very similar in both the $\epsilon = 1.4$ and $\epsilon = 5$ cases and because in the $\epsilon = 1.4$ case, the gap begins to widen rapidly above 1.2 km as the terrain flares outward toward the ridge crest.

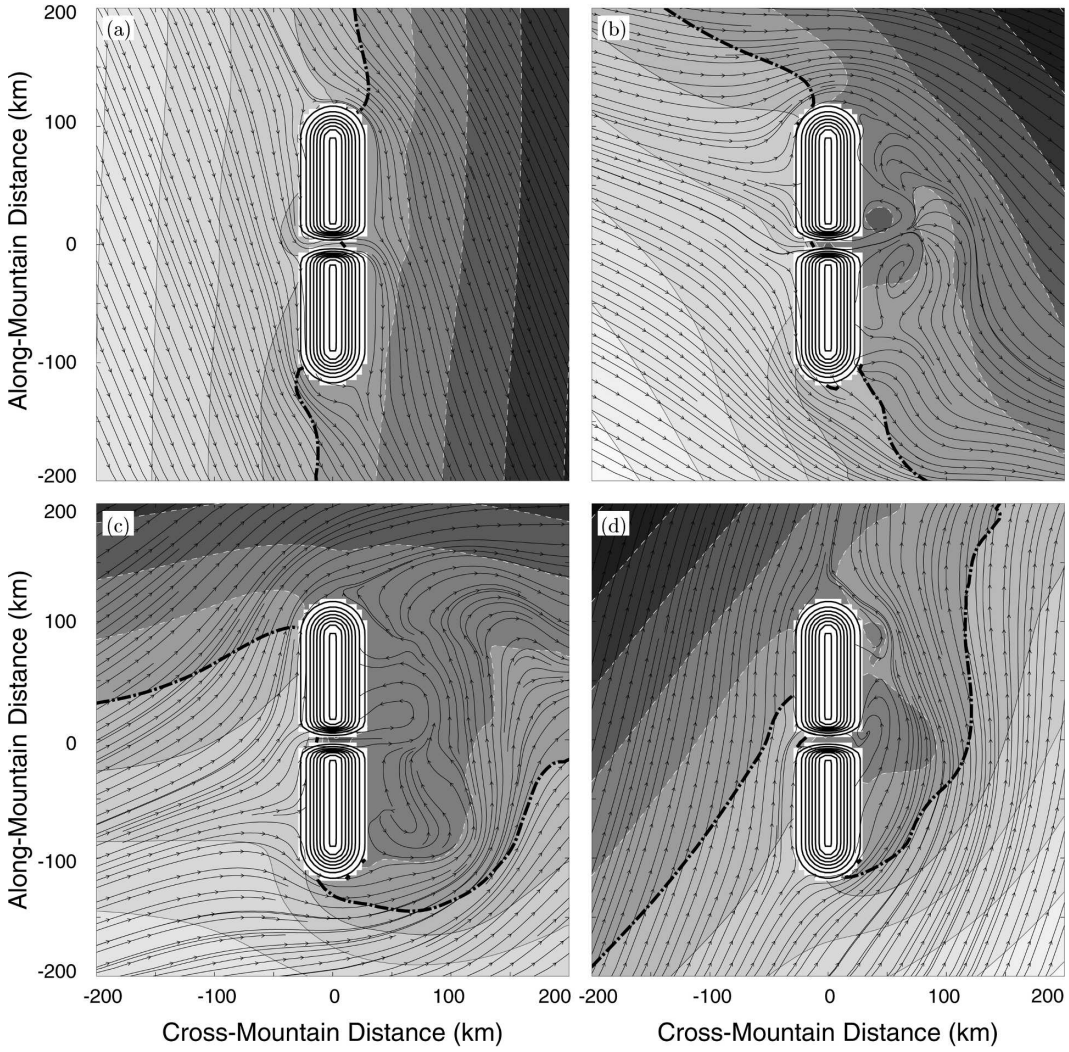

FIG. 7. Same as in Fig. 2 but for $\epsilon = 5.0$, CI = 30 Pa.

roughly 0.64 relative to the area of the upstream face of the upstream volume (and the downstream face of the downstream volume).

Mass flux budgets were calculated when the flow within the gap reached a quasi-stationary state, which occurred in all cases by $T = 40$. The mass flux budgets for all simulations close to within 10% of the largest individual term. The largest discrepancy occurred for the $\epsilon = 1.4$ SW case in which the wave-breaking region associated with the mountain wave produced over the southern slope of the gap (see Fig. 6) was not completely steady. In addition to nonsteadiness, the other factor that contributed to a nonzero residual was the interpolation from the terrain-following grid (on which the model is mass conservative) to a control volume with a horizontal upper boundary.

The budgets for the $\epsilon = 1.4$ and $\epsilon = 5$ simulations are shown in Figs. 10 and 11, respectively. For each simulation all terms appearing in (3)–(5) are normalized with division by $\max(|\phi^x_{\rightarrow \mathrm{en}}|, |\phi^x_{\rightarrow \mathrm{c}}|, |\phi^x_{\mathrm{c}\rightarrow}|, |\phi^x_{\mathrm{ex}\rightarrow}|)$ and plotted at representative locations along the x axis. The along-gap fluxes ϕ^x are plotted at the x coordinate of the y–z face through which the flux is transmitted, whereas the fluxes ϕ^y and ϕ^z are plotted at the x coordinate of the center of the surface through which they are transmitted. The ridge profile and the u component of the wind at the *surface*, averaged across the width of the gap, are also displayed below the budget data for each simulation.

In all eight simulations, the mass flux out of the upstream volume ($\phi^x_{\rightarrow \mathrm{c}}$) exceeds that coming in ($\phi^x_{\rightarrow \mathrm{en}}$), due, at least in part, to lateral convergence ($\phi^y_{\mathrm{en}} < 0$). Since the y–z cross-sectional area decreases by a factor of approximately 0.64 across the entrance volume, this

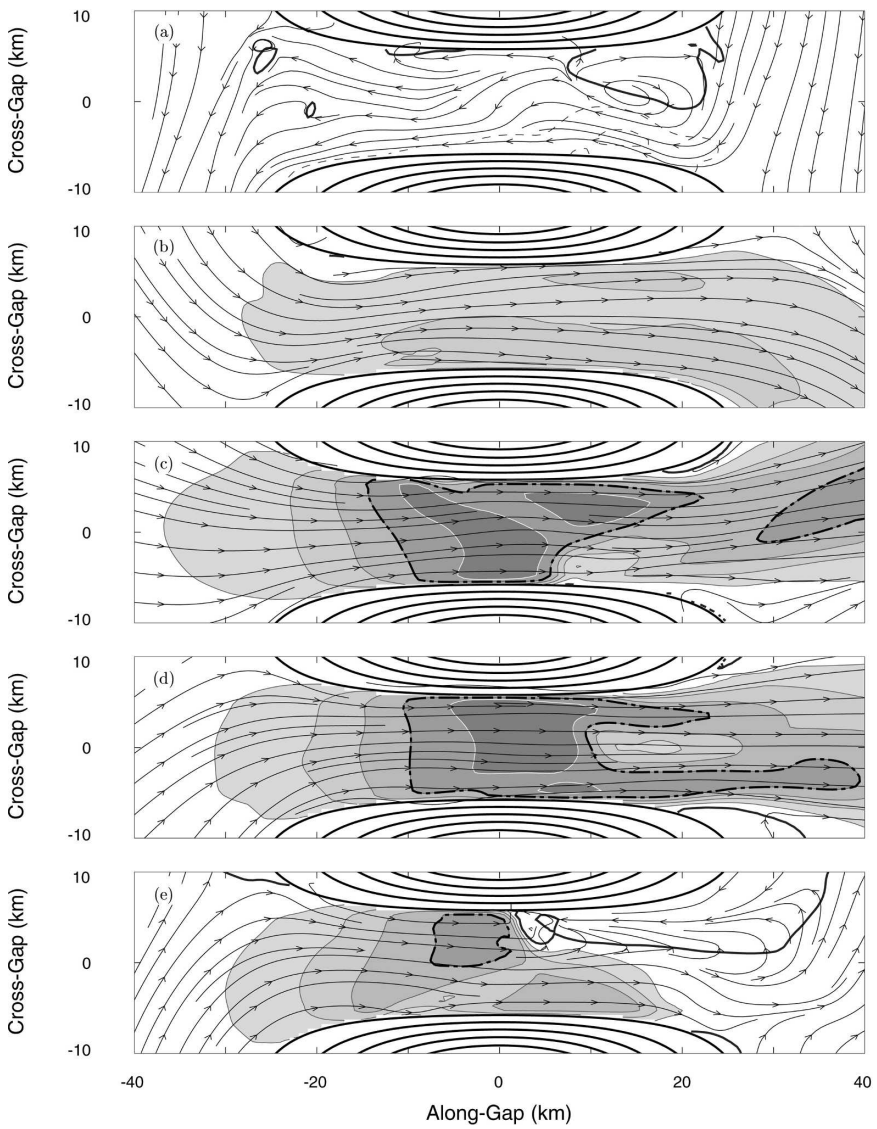

FIG. 8. Same as in Fig. 3 but for (a) a free-slip simulation and (b)–(e) with surface friction. The initial wind direction is from the (a) N, (b) N, (c) NW, (d) W, and (e) SW. Only the 2.5 and 5 m s^{-1} contours appear in (b).

downstream increase in mass flux implies a substantial increase in wind speed. The various cases do, however, differ significantly in the remaining details of their mass budgets.

The mass budgets for the simulations that produce the strongest gap winds, the $\epsilon = 1.4$ NW and W cases, are very similar to those for the mountain wave regime discussed in GD04. In particular, as shown in Fig. 10, there is a monotonic increase in the mass flux along the gap so that the average wind out the downstream face of the exit volume is roughly three times that entering the upstream volume. The mass flux continues to increase downstream due to mountain-wave-induced subsidence in the central volume and exit volume (ϕ_c^z, $\phi_{ex}^z < 0$). The subsidence in the exit volume is particularly strong. The normalized budgets for the $\epsilon = 1.4$ N and SW cases look roughly similar to each other and, in contrast to the NW and W cases, the mass flux in the upstream side of the entrance volume is almost identical to that out the downstream side of the exit volume, implying that the region of high winds is confined to within the gap itself (see also Fig. 5). Lateral divergence is responsible for this downstream deceleration of the gap winds in the exit region where, unlike the NW and W cases, the vertical mass fluxes are small.

In the N case with $\epsilon = 5$ the normalized mass budget

TABLE 1. Maximum surface winds in the gap and on the lee slope as a function of ϵ and large-scale wind direction. The relative enhancement is computed as $(|\mathbf{v}| - U)/U$, where $\mathbf{v}$ is the horizontal wind vector at $z = 10$ m and U is the large-scale geostrophic wind speed.

		Wind speed (m s^{-1})		Relative enhancement	
Initial conditions		Gap	Downslope	Gap	Downslope
			$U = 10$ m s^{-1}		
$\epsilon = 1.4$	N	8.5	—	−0.15	—
$h_0 = 1400$m	NW	12.75	15.0	0.275	0.5
	W	12.5	13.0	0.25	0.3
	SW	9.5	15.5	−0.05	0.55
			$U = 5.0$ m s^{-1}		
$\epsilon = 5.0$	N	3.1	—	−0.38	—
$h_0 = 2500$m	NW	9.0	5.0	0.8	0
	W	8.5	4.5	0.7	−0.1
	SW	7.0	5.0	0.4	0

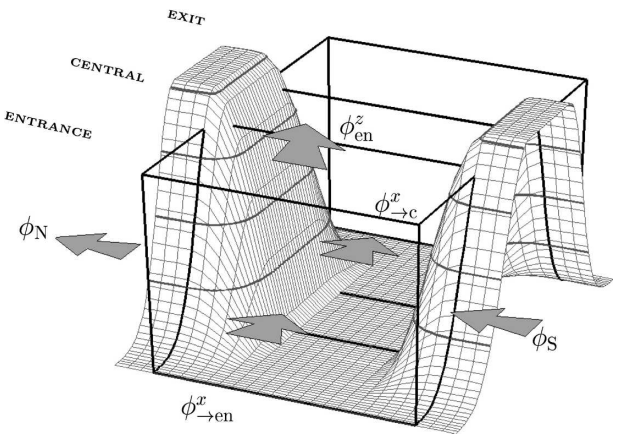

FIG. 9. Control volumes for analysis of the low-level mass budget in the gap. Arrows representing mass fluxes for the entrance region are also shown: $\phi^y_{\rm en} = \phi_N - \phi_S$.

shown in Fig. 11 is similar to that for the corresponding $\epsilon = 1.4$ simulation except that weak downward mass fluxes produce a weak acceleration within the central volume when $\epsilon = 1.4$, but not when $\epsilon = 5$. The overall mass budgets for SW flow are also similar in the $\epsilon = 5$ and $\epsilon = 1.4$ cases although, when $\epsilon = 5$, there is a small net acceleration of the downstream flow relative to that upstream of the gap. In contrast, the mass budgets for the $\epsilon = 5$ NW and W cases are quite different from those obtained when $\epsilon = 1.4$. Instead of the mountain wave regime, the budgets for the $\epsilon = 5$ NW and W cases resemble those for the upstream-blocking regime identified in GD04. After increasing in the entrance volume, the along-gap mass fluxes are relatively constant, which, due to the increase in cross-sectional area between the upstream and downstream faces of the exit volume, implies that the strongest winds are found within the gap. Vertical fluxes are relatively weak in these simulations, although not as weak as in the case examined in GD04. In particular, weak vertical fluxes contribute to the acceleration in the entrance volume in both the NW and W cases, and weak vertical accelerations contribute to a small reduction in the mass flux out of the exit volume in the W case.

5. Gap flow dynamics

Let us shift our focus closer to the surface and examine the x-momentum budget in the three control volumes shown in Fig. 12. The entrance, central, and exit volumes occupy the same regions along the x axis as those used previously for the momentum budget, but their width is reduced to the 10-km-wide region $|y| < d/2$ across which the bottom of the gap is essentially flat and the top of each volume is lowered to $z = 500$ m.

Neglecting the horizontal subgrid-scale momentum flux divergences $\partial\tau_{xx}/\partial x$ and $\partial\tau_{xy}/\partial y$, whose numerical values were in all cases negligible, the steady state x-momentum equation may be expressed as

$$\frac{\partial \rho u^2}{\partial x} + \frac{\partial \rho u v}{\partial y} + \frac{\partial \rho u w}{\partial z} + \frac{\partial p}{\partial x} + (-\rho f v) + \left(- \frac{\partial \tau_{xz}}{\partial z} \right) = 0. \tag{6}$$

The control volume integral of each term in the preceding is plotted for the $\epsilon = 1.4$ and $\epsilon = 5$ simulations in Figs. 13 and 14, respectively. All terms in the momentum budget for each simulation are normalized by dividing them by the magnitude of the largest single term in the budget.[2] The normalized values are plotted at the x coordinate of the centroid of the control volume over which they are computed. As implied by (6), those terms acting to increase the wind speed along the gap (i.e., to increase $\partial\rho u^2/\partial x$) are negative. In most cases the momentum budgets close to within 10% of the largest individual term; the exceptions are associated with nonsteady mountain wave activity in the gap exit volume. The maximum discrepancy occurs owing to wave breaking in the SW $\epsilon = 1.4$ case in which the residual is 17.6% of the largest individual term.

The increase in the *dimensional* along-gap momentum ($\partial\rho u^2/\partial x$) across the entrance volume is actually

[2] This normalization allows the results to be legibly displayed in a compact figure. The cross-gap-averaged wind speeds plotted at the bottom of each figure are indicative of the relative strengths of the dimensional accelerations.

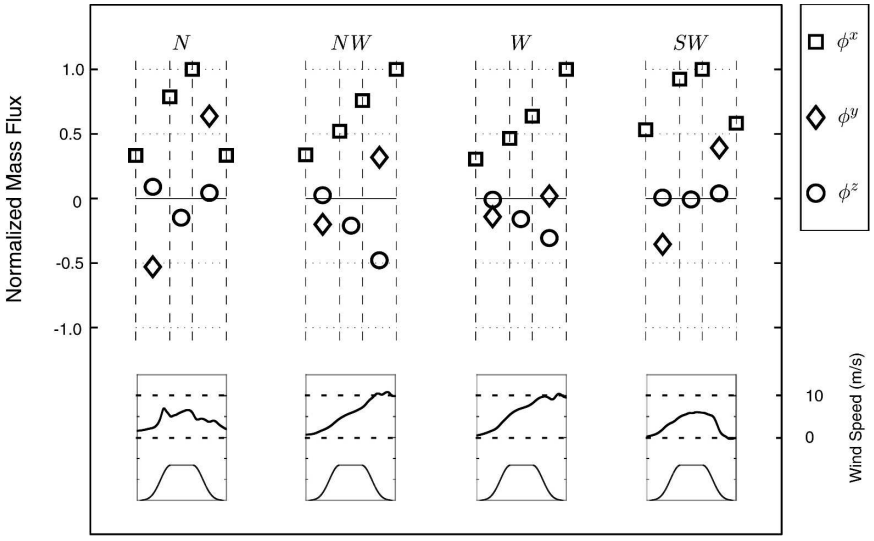

FIG. 10. Normalized mass fluxes in the control volume along the gap (Fig. 9) for flows with $\epsilon = 1.4$ at $T = 40$. (top) For each wind direction, the left-hand pair of lines delimits the entrance volume, the center pair the central volume, and the right-hand pair the exit volume. (bottom) The velocity component u at the surface averaged over the width of the gap along with a cross section of the ridge in which the gap is embedded. Squares, diamonds, and circles represent values of ϕ^x, ϕ^y, and ϕ^z, respectively.

very similar in all four $\epsilon = 1.4$ cases, although this is not apparent in the budget portion of Fig. 13 due to the normalization. The similarity in the acceleration across the entrance volume can, however, be seen in the across-gap-averaged surface winds plotted below each budget in Fig. 13. Both pressure gradient forces and lateral momentum flux convergence contribute to this acceleration, with the relative importance of each factor differing between the various cases. In all cases and in all volumes the contribution from the Coriolis force is small, and that from surface friction is somewhat larger but never dominant and is always decelerative. Nevertheless, as previously discussed, surface friction plays an important indirect role in the N case by turning the low-level flow to produce upstream blocking along the eastern side of the ridge. As a consequence, in the N case the actual pressure gradient in the entrance volume is double the synoptic-scale gradient.

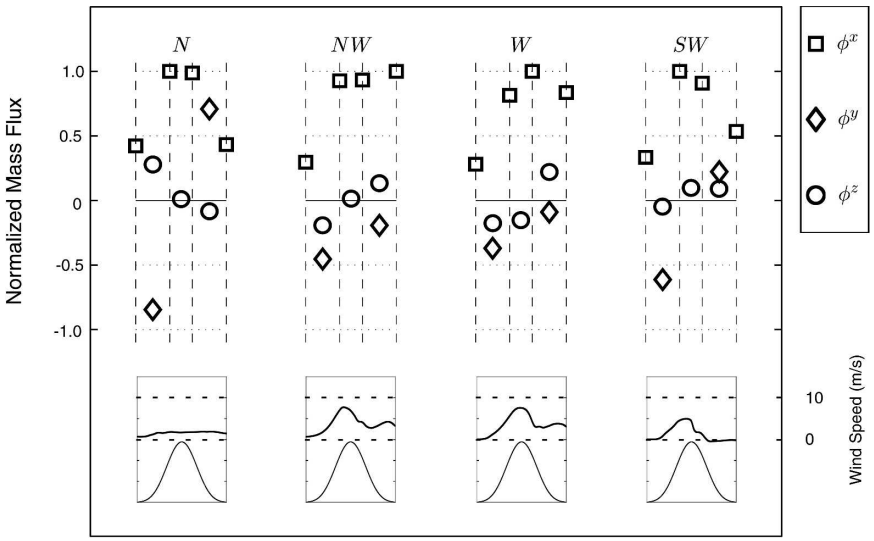

FIG. 11. Same as in Fig. 10 except for $\epsilon = 5.0$.

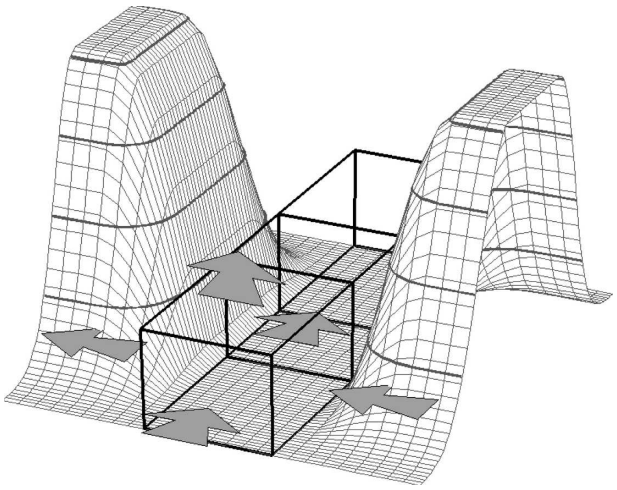

FIG. 12. Same as in Fig. 9 but for the momentum budget. Arrows represent advection through the faces of the entrance volume.

The along-gap momentum continues to increase across the central volume in all four $\epsilon = 1.4$ simulations (Fig. 13). In the N, NW, and W cases, pressure gradient forces are a major contributor to this acceleration with some additional contribution from vertical momentum flux convergence (i.e., downward fluxes of momentum through the top of the control volume). In the SW case, on the other hand, the central volume acceleration is primarily forced by lateral momentum flux convergence associated with downslope flow into the gap as illustrated in Fig. 6, and the vertical fluxes are decelerative. The $\epsilon = 1.4$ NW and W cases (the mountain wave regime cases) are the only simulations in which the along-gap momentum continues to increase across the exit volume. The acceleration in the exit volume is forced by strong downward momentum flux convergence and to a lesser extent by the pressure gradient force, and is opposed by lateral momentum flux divergence and surface friction. Net deceleration in the gap exit region is produced in the other cases, primarily by lateral momentum flux divergence and surface friction in the N case and by vertical flux divergence and pressure gradient forces in the SW case.

As when $\epsilon = 1.4$, the along-gap momentum also increases across the entrance volume in all of the $\epsilon = 5$ cases. The *dimensional* acceleration is, however, much weaker in the N case, as indicated by the surface wind speed plots. Whereas the synoptic-scale winds and pressure gradients are reduced by one-half between the $\epsilon = 1.4$ and $\epsilon = 5$ cases, the surface winds in the gap are reduced by almost two-thirds (Table 1). This is probably due to the previously discussed tendency for the split flow in the free-slip $\epsilon = 5$ case to develop a weak westward pressure gradient within the gap (see Fig. 8a), which must then be overcome by frictional turning and blocking of air along the western side of the ridge.

Pressure gradient forces along with both vertical and lateral momentum flux convergence all play a role in the entrance-region acceleration in the stronger NW,

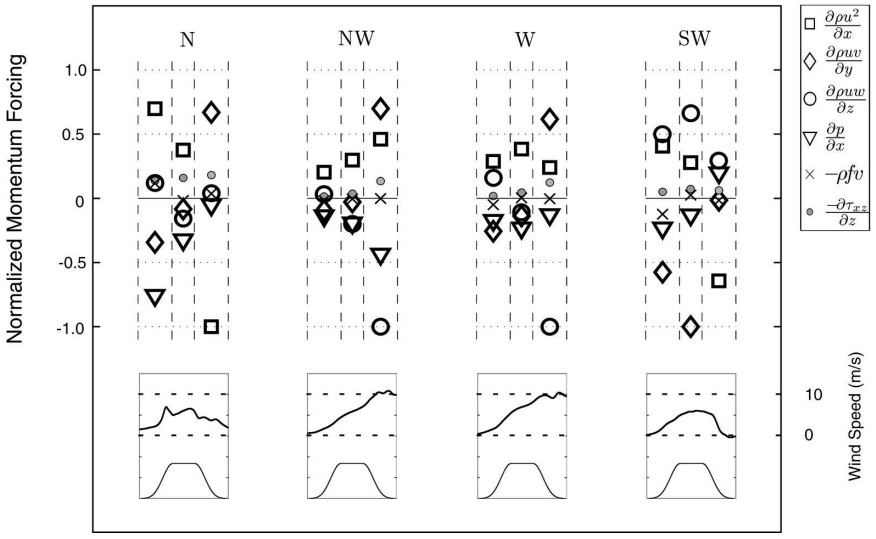

FIG. 13. As in Fig. 10 but for momentum budget terms averaged over the control volumes in Fig. 12. Vertical dashed lines denote the x-coordinate locations of the boundaries of the individual control volumes. Squares, diamonds, circles, triangles, crosses, and small circles denote the volume integrals of $\partial \rho u^2/\partial x$, $\partial \rho uv/\partial y$, $\partial \rho uw/\partial z$, $\partial p/\partial x$, $-\rho fv$, and $-\partial \tau_{xz}/\partial z$, respectively.

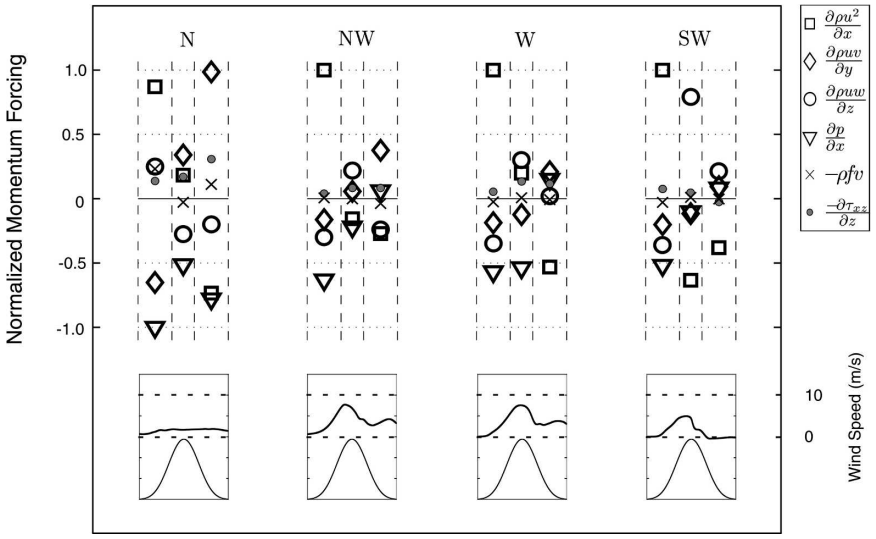

FIG. 14. Same as in Fig. 13 except for $\epsilon = 5.0$.

W, and SW cases. The pressure gradient force continues to be accelerative in the central volume in all four cases, but actual acceleration within this volume only occurs in the W and N cases. Deceleration, primarily forced by vertical momentum flux divergence, is found in the central volume for the NW and SW cases. Deceleration occurs in the exit volume in all cases. This is primarily associated with lateral momentum flux divergence along with adverse pressure gradients in the NW, W, and SW cases. Vertical momentum flux divergence is also a significant decelerative forcing in the SW case. The general character of the momentum budgets for the three $\epsilon = 5$ westerly flow cases is similar to that for the upstream-blocking regime in GD04, particularly in the region of flow acceleration at the gap entrance. Nevertheless, vertical momentum fluxes play a larger role in these simulations than for the prototypical upstream-blocking case examined in GD04.

6. Flow in a very long gap

The dynamics and kinematics of the gap flows in the previous simulations were dramatically influenced by mesoscale circulations in the entrance and exit regions. Many idealized models of gap flow neglect the entrance and exit entirely and focus on the response of a fluid in an infinite channel to a mean along-gap pressure gradient (Overland and Walter 1981; Mass et al. 1995). Flow close to this idealization may be obtained when the geostrophic wind is northerly (so there is a west-to-east large-scale pressure gradient) and the gap is very long. Here we examine the vertical motions and the mass and momentum balances in such a flow. The simulation is identical to the $\epsilon = 1.4$ N case except that the x-dimension of the flat top on the ridge was extended from 20 to 140 km, which is roughly similar to the length of the Columbia River Gorge on the border between Washington and Oregon. This is not, however, an idealized simulation of a prototypical gap flow in the gorge since there is only a minimal difference between the temperatures of the air masses at each end of the gap (Sharp 2005).

The mass and momentum budgets in the central part of the gap were evaluated using four control volumes, each 26 km in length with the interface between volumes 2 and 3 located at the center of the gap ($x = 0$). The tops and lateral sides of these volumes are identical to those used in the central volumes in the previous mass and momentum budget analyses. The locations of these control volumes relative to the full length of the uniform portion of the long gap are indicated by Roman numerals in Fig. 15a.

Figure 15a shows $\overline{u}$, the cross-gap average of the along-gap wind, at $z = 10$ m, 400 m, and 1200 m as a function of x. Each value of $\overline{u}$ is obtained by averaging u across the gap over the width of the control volumes used in the momentum budget calculations ($-4.5 \leq y \leq 4.5$ km). Rapid changes in wind speed are evident near each end of the gap, but the gradient in $\overline{u}$ is relatively uniform over the four control volumes. At $z = 10$ m $\overline{u}$ increases only slightly from 3 m s^{-1} at the upstream face of volume I to 4 m s^{-1} at the downstream face of volume IV. Both wind speed and the along-gap acceleration increase with height. The level of maximum along-gap winds is near $z = 400$ m, at which level $\overline{u}$ increases from 5 to 10 m s^{-1} over the length of the

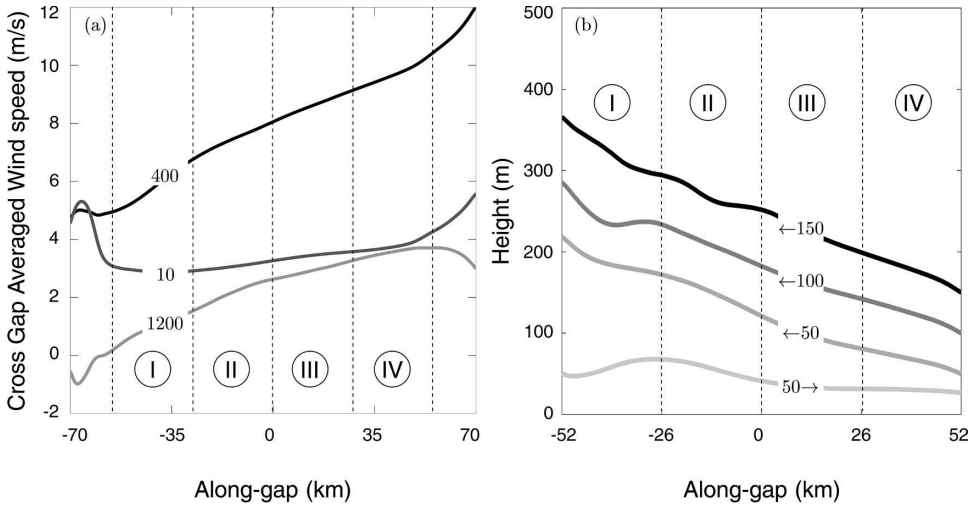

FIG. 15. (a) The u component of velocity, averaged over the gap width of $-4.5 \leq y \leq 4.5$ km at three different heights: 400, 10, and 1200 m, as a function of distance in the long gap. (b) Average of the x–z projection for nine individual trajectories terminating at cross-gap coordinates $y = -2.0, -1.5, \ldots, 2.0$ km. Three are for backward (←) trajectories terminating at $x = 52$ km and heights 50, 100, and 150 m and one is for forward (→) trajectories starting at $x = -52$ km, $z = 50$ m.

control volumes. Nearer the top of the gap, at $z = 1200$ m (the top of the control volumes used in the mass budget), the upstream $\overline{u}$ are much weaker but still undergo a significant acceleration down the gap.

The mass budget within these four control volumes is shown in Fig. 16a. The along-gap mass flux increases at an almost uniform rate across each control volume, which is consistent with the almost uniform rate at which the across-gap averages of u increase downstream in Fig. 15a. Since the sides of the mass budget volumes extend to the walls of the gap, there are no lateral mass fluxes and the increase in mass flux downstream is produced by subsidence from aloft.

The along-gap momentum flux also increases downstream (Fig. 16b) although, due to the smaller y–z cross section of the control volumes, the increases are less uniform than those for the mass flux. The biggest contributor to this acceleration is the pressure gradient force (consistent with the concept of pressure driven channeling) although, unlike the constant gradient in the geostrophically balanced large-scale pressure field, the actual pressure gradient force increases downstream and is weaker than the large-scale gradient except near the exit. Weak mountain waves forced by the northerly flow across the upper shoulders of the gap are responsible for this mesoscale variation in the pressure gradient force.

Another important term in the momentum budget is the vertical divergence of the subgrid-scale momentum flux, which is the difference between the turbulent subgrid-scale transport at the top of the control volume and surface friction at the bottom. The turbulent fluxes aloft are negligible compared to surface friction (less than 3% of the total dissipation term) because the vertical shear in horizontal wind is much stronger near the surface.

Mass et al. (1995) suggested that the momentum budget for winds in a long, straight, narrow gap is dominated by a three-term balance involving acceleration, pressure gradient forces, and surface friction. Colle and Mass (2000), on the other hand, found much more complex balances in pointwise momentum budgets from an MM5 simulation of gap winds in the Strait of Juan de Fuca, although at least some of the complexity was associated with the complex structure of the real terrain. Yet even in the interior of this idealized gap, the balance is relatively complicated. Except in the first control volume, lateral momentum flux convergence has the same magnitude but opposite sign as the surface friction. Vertical momentum flux convergence also tends to accelerate the flow, although in volume I, its contribution is small. Recall that subsidence plays an extremely important role in the mass budget (Fig. 16a), the control volumes for which extend all the way to each sidewall and up to $z = 1200$ m. On the other hand, the momentum flux control volumes are limited to the center section of the gap where the topography is flat and only extend up to $z = 500$ m. The lateral momentum fluxes in Fig. 16b appear to be the result of gentle downward momentum transport over the entire lateral width of the gap, which is subsequently forced toward the centerline by the sidewalls.

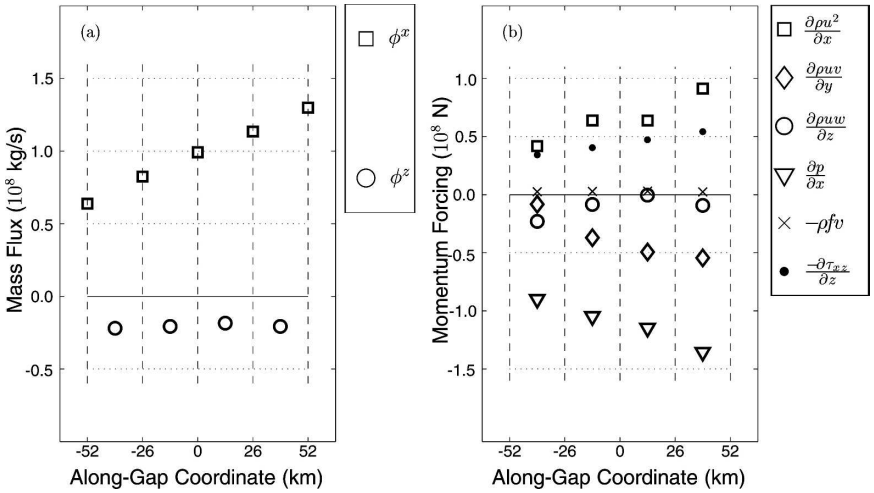

FIG. 16. The (a) mass and (b) momentum budget for the four control volumes in the center of the long gap: notation as in Fig. 10 for mass and Fig. 13 for momentum.

The importance of subsidence is illustrated by the cross-gap-averaged backward trajectories plotted in Fig. 15b, which terminate at heights of 50, 100, and 150 m. Each of these curves is the average height, as a function of x, of nine individual backward trajectories terminating at the downstream face of volume IV (x = 52 km), the specified vertical level, and one y location in the set [−2, −1.5, −1, . . . , 2 km]. Significant descent is clearly a pervasive feature of the flow. Sharp (2005) has found similar subsidence in high-resolution simulations of actual Columbia Gorge events. Of course, air parcels originating sufficiently near the surface undergo significantly less descent, as indicated in Fig. 15 by the cross-gap-averaged forward trajectory originating at z = 50 m. This curve is computed in the same manner as the cross-gap-averaged backward trajectories except that the nine trajectories included in the average originate at the upstream face of volume I (x = −52 km).

7. Conclusions

We have investigated the relative importance of synoptic-scale and mesoscale forcing in driving idealized flows through a level gap in an isolated mountain. Above the boundary layer, the synoptic-scale winds were uniform and in geostrophic balance. The ridge ran north–south and the gap east–west so that the direction of gap winds forced by the large-scale pressure gradient varied systematically as the synoptic-scale wind changed between northerly, northwesterly, westerly, and southwesterly. In all cases, mesoscale circulations associated with mountain waves or upstream blocking tended to create along-gap pressure gradients quite different from those associated with the large-scale geostrophically balanced flow.

For free-slip northerly flow (with both ϵ = 1.4 and 5), the along-gap synoptic-scale pressure gradient was unable to generate gap flow through the mechanism of pressure driven channeling. This is consistent with Zängl (2002a), who found that surface friction is crucial for the development of gap flows. Surface friction turns the low-level flow toward the eastern side of the ridge, enhancing the cross-gap pressure perturbation through upstream blocking. As a consequence, in the ϵ = 1.4 case, the total pressure gradient within the gap entrance region was roughly twice the strength of the synoptic-scale pressure gradient. The mesoscale enhancement of the pressure gradient in the entrance region was much less in the ϵ = 5 case since it is opposed by the pressure gradient that develops as a result of the flow splitting and Coriolis forces in the free-slip case (Zängl 2002a). Surface friction also helped generate gap flow by simply decoupling the flow low in the gap from the northerlies along the ridge top in the ϵ = 1.4 case, but this mechanism was not important when ϵ = 5 because, even in the free-slip case, nonlinear processes decouple the low-level split flow from that aloft.

For each mountain height investigated in this study, stronger gap winds developed when the upstream wind had a westerly component. Among all of the cases, the strongest gap winds were produced in the northwesterly and westerly simulations with the 1.4 km mountain (ϵ = 1.4). The processes responsible for the strong winds are identical to those identified for the *mountain wave* regime in the nonrotating free-slip simulations presented in GD04; downward mass and momentum fluxes near

the gap exit were the dominant processes creating the high winds. Note that in the mountain wave cases, the strength of the gap winds was still exceeded by the strength of downslope winds along the lee slopes of the topography (Table 1). The southwesterly case was weaker than the northwesterly and westerly cases because surface friction turned the low-level flow to almost southerly, and the mountain waves triggered by the main north–south crest were therefore weaker. Strong southwesterly downslope winds did, however, develop along the upper sides of the southern flank of the gap.

When the mountain height increased to 2.5 km and the upstream wind was reduced from 10 to 5 m s^{-1}(ϵ = 5), the gap winds were weaker, and in the three westerly wind cases the situation was similar to the "upstream-blocking" regime identified in GD04, with the strongest accelerations occurring near the gap entrance due to pressure gradient forces induced by flow blocking. In contrast to the ϵ = 1.4 cases, when ϵ = 5 the winds in the gap are stronger than those on the lee slopes (Table 1). The enhancement of the gap winds relative to the background geostrophic wind is also stronger when ϵ = 5 but, since such high values of ϵ are only likely to occur under meteorological conditions with weak ambient winds, the upstream-blocking regime is not likely to generate genuinely strong gap winds in real-world events.

These results, taken together with previous studies by Colle and Mass (2000), Zängl (2002a,b), and GD04, suggest that mesoscale circulations forced by the mountain itself and by the topography near each end of the gap play a very important role in the dynamics of gap winds. Nevertheless, one might suppose that the dynamics are different near the center of a very long gap. The flow near the center of such a long gap was investigated by increasing the length of the uniform gap in the ϵ = 1.4 north-flow case from 20 to 140 km.

The kinematics and dynamics of the simulated flow in the center of the long straight gap were indeed different than those active near the ends of the gap. Even within the center of the long gap, however, the dynamics are not that of a horizontal flow in which acceleration is balanced by the pressure gradient force (Overland and Walter 1981) or the pressure gradient force and surface friction (Mass et al. 1995). The across-gap-averaged trajectories show significant descent over the central 100 km of the gap and subsidence plays a major role in the mass balance within the gap. In the lowest part of the gap, lateral momentum flux convergence forced by downward momentum fluxes farther aloft typically has the same magnitude in the momentum budget as surface friction. These results suggest that subsidence, identified in GD04 as crucial for the development of gap winds in the mountain wave regime, continues to play a significant role in much weaker cases without significant cross-ridge flow.

As mentioned in the introduction, in many real-world gap flows the cross-mountain synoptic-scale pressure gradient includes a component produced by large temperature contrasts in the low-level air masses on each side of the mountain. The influence of such cross-barrier temperature differences has been neglected in this study, which focused exclusively on synoptic-scale pressure gradients that are in geostrophic balance with the upper-level flow. The more general case is difficult to treat in an idealized framework and is beyond the scope of this paper. Nevertheless, observations and case study simulations of Colle and Mass (2000) suggest that the basic results from these idealized simulations carry over to at least some real-world gap winds in the Strait of Juan de Fuca. Sharp (2005) has also recently demonstrated the importance of subsidence and mountain waves in creating high winds near the exit of the Columbia River Gorge.

Acknowledgments. This research was supported by National Science Foundation Grants ATM-0137335 and ATM-0506589. The authors benefited from illuminating conversations with Cliff Mass and Justin Sharp, and from comments by three anonymous reviewers.

APPENDIX A

Geostrophic Balance in the Initial State

The full equations for the free-slip, $f = 0$, version of the numerical model are given in GD04. In this paper the horizontal components of the Coriolis force are included in the horizontal momentum equations through the standard f plane approximation with $f = 10^{-4}$ s^{-1}. The initial state, in the absence of topography, consists of hydrostatic and geostrophically balanced fields of pressure and potential temperature.

The model solves the governing equations written in terms of the Exner function $\pi = (p/p_0)^{R/c_p}$ and the potential temperature θ. Using these variables, the geostrophic wind satisfies

$$u_g = -\frac{c_p}{f}\,\theta\,\frac{\partial \pi_g}{\partial y} \tag{A1}$$

$$v_g = \frac{c_p}{f}\,\theta\,\frac{\partial \pi_g}{\partial x}, \tag{A2}$$

where π_g is the geostrophically balanced perturbation with respect to a horizontally uniform hydrostatically

balanced reference pressure $\pi_0(z)$. The thermal wind equation for the π–θ system is

$$f\left(\frac{\partial}{\partial z} - \frac{N^2}{g}\right)u_g = -\frac{g}{\theta_g}\frac{\partial \theta_g}{\partial y} \tag{A3}$$

$$f\left(\frac{\partial}{\partial z} - \frac{N^2}{g}\right)v_g = \frac{g}{\theta_g}\frac{\partial \theta_g}{\partial x}, \tag{A4}$$

where the preceding defines $\theta_g(x, y, z)$ as the potential temperature in thermal wind balance with the geostrophic wind.

Although there is no vertical shear in the geostrophic wind in the cases discussed in this paper, weak horizontal gradients in θ_g must be present to satisfy the thermal wind balance in the π–θ system. This was achieved by setting $\theta_g(0, 0, z) = \theta_0(z)$, where $\theta_0(z)$ is in hydrostatic balance with $\pi_0(z)$, and integrating

$$\frac{\partial \theta_g}{\partial y} = \frac{N^2 f \theta_g}{g^2} u_g$$

$$\frac{\partial \theta_g}{\partial x} = -\frac{N^2 f \theta_g}{g^2} v_g$$

outward from $(x, y) = (0, 0)$ on each vertical level within the numerical domain. As a last step, at every horizontal location $(x, y) = (r\Delta x, s\Delta y)$, $\pi_g(r\Delta x, s\Delta y, z)$ was computed by integrating the hydrostatic equation from the surface to the top of the domain. Note that this procedure will also work if there is a uniform vertical shear in the geostrophic wind.

The required changes to the mathematical model are to replace the buoyancy term in Eq. (1) of GD04 by

$$+\epsilon_{ijk} f \delta_{j3} u_k - \delta_{i3} g \frac{\theta - \theta_g}{\theta_g}.$$

Here δ_{ij} and ϵ_{ijk} are the Kronecker delta and the alternating tensor, respectively, and θ_g appears in the buoyancy term because it represents that part of the potential temperature in hydrostatic balance with the pressure field.

APPENDIX B

Surface Friction

The boundary layer parameterization is based on a simplified version of Blackadar's first-order closure described by Zhang and Anthes (1982). It uses an explicit "surface level" at a fixed height ($z_s = 10$ m) regardless of the vertical grid spacing (Δz). Three additional 2D variables were introduced on this level (u_s, v_s, θ_s). The parameterization is limited to cases with a neutral and stably stratified boundary layer. The surface heat flux is set to zero by assuming that the ground temperature equals that of the air at the level z_s.

First, the friction velocity u_* and the ground stress τ_s are calculated as

$$u_* = \frac{\kappa |\mathbf{u}_s|}{\ln(z_s/z_0)}$$

$$\tau_s = \rho u_*^2,$$

where $\kappa = 0.4$ is von Kármán's constant and z_0 is surface roughness. To determine the subgrid-scale mixing coefficient (eddy diffusivity $\mathcal{K}_s$ at the lowest level z_s) we first need to compute components (D_{ij}) using the information from the surface level (z_s) and first regular model level ($k = 1$). In the next step, the static stability N_s^2 of the layer between the two aforementioned levels is calculated. Then $\mathcal{K}_s$ is calculated in the same manner as for the other model levels with the exception that Δ^2 used at other vertical levels ($\Delta z \cdot \Delta z$) was replaced by l^2 where l represents a typical scale of eddies that carry the most energy. We chose $l = 40$ m to be the difference between the first regular vertical level ($z = 50$ m) and the surface level ($z_s = 10$ m). The surface variables (u_s, v_s, θ_s) are finally integrated forward in time [Eq. (B1)] using a trapezoidal scheme to ensure numerical stability:

$$\frac{\partial u_s}{\partial t} = \frac{\mathcal{K}_s \dfrac{u_1 - u_s}{z_1 - z_s} - \dfrac{\tau_s}{\rho}\dfrac{u_s}{|\mathbf{u}_s|}}{\dfrac{1}{2}(z_1 - z_s)}$$

$$\frac{\partial v_s}{\partial t} = \frac{\mathcal{K}_s \dfrac{v_1 - v_s}{z_1 - z_s} - \dfrac{\tau_s}{\rho}\dfrac{v_s}{|\mathbf{u}_s|}}{\dfrac{1}{2}(z_1 - z_s)} \tag{B1}$$

$$\frac{\partial \theta_s}{\partial t} = \frac{\mathcal{K}_s \dfrac{\theta_1 - \theta_s}{z_1 - z_s}}{\dfrac{1}{2}(z_1 - z_s)},$$

where the subscript "1" denotes values on the first regular grid level (at height $\Delta z/2$).

REFERENCES

Colle, B. A., and C. F. Mass, 1998a: Windstorms along the western side of the Washington Cascade Mountains. Part I: A high-resolution observational and modeling study of the 12 February 1995 event. *Mon. Wea. Rev.,* **126,** 28–52.

——, and ——, 1998b: Windstorms along the western side of the Washington Cascade Mountains. Part II: Characteristics of past events and three-dimensional idealized simulations. *Mon. Wea. Rev.,* **126,** 53–71.

——, and ——, 2000: High-resolution observations and numerical simulations of easterly gap flow through the Strait of Juan de

Fuca on 9–10 December 1995. *Mon. Wea. Rev.,* **128,** 2398–2422.

Colman, B. R., and C. F. Dierking, 1992: The Taku wind of southeast Alaska: Its identification and prediction. *Wea. Forecasting,* **7,** 49–64.

Flamant, C., and Coauthors, 2002: Gap flow in an Alpine valley during a shallow south föhn event: Observations, numerical simulations and hydraulic analogue. *Quart. J. Roy. Meteor. Soc.,* **128,** 1173–1210.

Gaberšek, S., and D. Durran, 2004: Gap flows through idealized topography. Part I: Forcing by large-scale winds in the nonrotating limit. *J. Atmos. Sci.,* **61,** 2846–2862.

Gohm, A., and G. Mayr, 2004: Hydraulic aspects of föhn winds in an Alpine valley. *Quart. J. Roy. Meteor. Soc.,* **130,** 449–480.

Jackson, P. L., and D. G. Steyn, 1994a: Gap winds in a fjord. Part I: Observations and numerical simulations. *Mon. Wea. Rev.,* **122,** 2645–2665.

——, and ——, 1994b: Gap winds in a fjord. Part II: Hydraulic analog. *Mon. Wea. Rev.,* **122,** 2666–2676.

Lackmann, G. M., and J. E. Overland, 1989: Atmospheric structure and momentum balance during a gap-wind event in Shelikof Strait, Alaska. *Mon. Wea. Rev.,* **117,** 1817–1833.

Mass, C. F., S. Businger, M. D. Albright, and Z. A. Tucker, 1995: A windstorm in the lee of a gap in a coastal mountain barrier. *Mon. Wea. Rev.,* **123,** 315–331.

Ólafsson, H., and P. Bougeault, 1997: The effect of rotation and surface friction on orographic drag. *J. Atmos. Sci.,* **54,** 193–210.

Overland, J. E., and B. A. Walter Jr., 1981: Gap winds in the Strait of Juan de Fuca. *Mon. Wea. Rev.,* **109,** 2221–2233.

Saito, K., 1993: A numerical study of the local downslope wind "Yamaji-kaze" in Japan. Part 2: Non-linear aspect of the 3-d flow over a mountain range with a col. *J. Meteor. Soc. Japan,* **71,** 247–271.

Sharp, J., 2005: The structure and dynamics of Columbia Gorge gap flow revealed by high-resolution numerical modeling. Ph.D. thesis, University of Washington, 190 pp.

——, and C. F. Mass, 2004: Columbia Gorge gap winds: Their climatological influence synoptic evolution. *Wea. Forecasting,* **19,** 970–992.

Smedman, A.-S., and H. Bergström, 1995: An experimental study of stably stratified flow in the lee of high mountains. *Mon. Wea. Rev.,* **123,** 2319–2333.

Sprenger, M., and C. Schär, 2001: Rotational aspects of stratified gap flows and shallow foehn. *Quart. J. Roy. Meteor. Soc.,* **127,** 161–187.

Steenburgh, J. W., D. M. Schultz, and B. A. Colle, 1998: The structure and evolution of gap outflow over the Gulf of Tehuantepec, Mexico. *Mon. Wea. Rev.,* **126,** 2673–2691.

Whiteman, C. D., and J. C. Doran, 1993: The relationship between overlying synoptic-scale flows and winds within a valley. *J. Appl. Meteor.,* **32,** 1669–1682.

Zängl, G., 2002a: Idealized numerical simulations of shallow föhn. *Quart. J. Roy. Meteor. Soc.,* **128,** 431–450.

——, 2002b: Stratified flow over a mountain with a gap: Linear theory and numerical simulations. *Quart. J. Roy. Meteor. Soc.,* **128,** 927–950.

——, 2004: Upstream effects of an Alpine-scale mountain range under various flow angles. *Meteor. Z.,* **13,** 291–296.

Zhang, D., and R. A. Anthes, 1982: A high-resolution model of the planetary boundary layer—Sensitivity tests and comparisons with SESAME-79 data. *J. Appl. Meteor.,* **21,** 1594–1609.